PERGAMON

International Journal of Heat and Mass Transfer 44 (2001) 2247–2260

International Journal of HEAT and MASS TRANSFER

www.elsevier.com/locate/ijhmt

Numerical simulation of mixed convection heat and mass transfer in a human inhalation test chamber

S. Hyun, C. Kleinstreuer *

Department of Mechanical and Aerospace Engineering, North Carolina State University, Campus Box 7910, 3211 Broughton Hall, Raleigh, NC 27695-7910, USA

Received 1 March 2000; received in revised form 1 August 2000

Abstract

Large baffled rectangular chambers, Rochester-style test chambers, and displacement ventilated rooms have traditionally been used to study effects of potentially toxic pollutants on animals and humans. Recently, the interest in harmful effects of *indoor* gaseous pollutants and associated air quality control have rapidly increased because most urban dwellers spend more than 90% of their daily lives in closed environments. Of interest here are the experimentally validated CFD simulations of transient turbulent non-isothermal flow with tracer gas transport in a personal exposure environment. The purpose of this paper is to examine the effect of transient breathing on trace gas ambient (i.e., exposure) concentrations and ultimately the uptake (i.e., dose concentrations) by the subject for three different orientations with respect to the non-isothermal air stream and the location of the tracer gas source.

1. Introduction

Large baffled rectangular chambers, Rochester-style test chambers, and displacement ventilated rooms have traditionally been used to study effects of potentially toxic pollutants on animals [1,2] and humans [3–5]. Recently, the interest in harmful effects of *indoor* gaseous pollutants and associated air quality control have rapidly increased [5,6] because most urban dwellers spend more than 90% of their daily lives in closed environments, e.g., homes, cars, offices, factories, public buildings, entertainment places, etc. [7]. Although there are many studies related to outdoor air quality prediction and control, their findings cannot be directly applied to the solution of indoor air pollution problems. Toward the end of the 1970s, it was recognized that there is a potential respiratory hazard in buildings – especially livestock buildings, factories and public buildings which are developed towards larger, higher mechanized, and often closed systems.

Traditional methods for designing air distribution in buildings are mainly based on semi-empirical relations, which do not include the effects of room geometry and occupants. Recently, with the availability of advanced computational fluid dynamics (CFD) simulation programs and computer-aided design (CAD) tools, air movement in ventilated enclosures has been studied in more detail [8,9]. For example, Topps et al. [10] calculated the contaminant distribution reasonably well in rooms with steady flow, for a known trace gas emission, but without occupants. In experimental studies contaminant distributions in ventilating rooms were investigated especially in the breathing zone, in order to obtain personal exposure data [10,11]. The smoke dispersion from human exhalation, and the interaction taking place between respiration and the convective boundary layer flow induced by the human body was simulated experimentally as well as computationally [6,12,13]. Full scale inhaling or exhaling thermal manikins (breathing thermal manikin, BTM) were used to study experimentally and computationally the personal contaminant exposure due to interacting air flows between two persons [13]. They [13] reported computational difficulties and CFD simulations were limited to

* Corresponding author Tel.: +1-919-515-5261; fax: +1-919-515-7968.

E-mail address: ck@eos.ncsu.edu (C. Kleinstreuer).

0017-9310/01/$ - see front matter
PII: S0017-9310(00)00268-4

Nomenclature

C_d	personal dose or exposure concentration (kg/m^3)
C_d^*	dimensionless parameter for personal dose or exposure
$\overline{C}_d^*$	time-averaged personal dose or exposure
$C_{d,st}^*$	steady-state personal dose or exposure
C_{ex}	fully mixed exit gas concentration (kg/m^3)
$C_\mu, C_{\varepsilon 1}, C_{\varepsilon 2}$	turbulence constants for the RNG k–ε model
D_{CO}	diffusion coefficient of CO in air (m^2/s)
D_h	hydraulic diameter (m)
Gr	Grashof number ($g\beta\Delta TL^3/v^2$)
g	gravity (m/s^2)
h	enthalpy (J/kg)
h_{BTM}	height of the breathing thermal manikin (BTM)
h_{mouth}	mouth height
k	turbulence kinetic energy (m^2/s^2)
L	length scale for the Grashof number (m)
p	pressure (Pa)
$\hat{Q}$	air flow rate at inlet (m^3/s)
q_j	heat flux (W/m^2)
Re_{D_h}	Reynolds number based on hydraulic diameter
Ri	Richardson number (Gr/Re^2)
S	rate of creation of mass per unit volume (kg/m^3 s)
Sc_t	turbulent Schmidt number (v_t/D_{CO})
S_p	pollutant gas strength (kg/s)
$\bar{S}_{ij}$	mean rate-of-strain tensor (1/s)
s	length scale (m)
T	temperature (K)
T_{pulse}	period of breathing (s)
T_{ref}	buoyancy reference temperature (K)
t	time (s)
U_{in}	inlet velocity (m/s)
u_i	velocity components in Cartesian coordinates (m/s)
u'	turbulence fluctuating velocity (m/s)
V_{tidal}	tidal volume (m^3)
x, y, z	Cartesian coordinates (m)
Y_{CO}	mass concentration of CO (kg/m^3)

Greek symbols

β_t	thermal expansion coefficient (1/K)
ε	turbulence dissipation rate (m^2/s^3)
η, η_∞, β	additional turbulence model constants
φ	inclined wall angle to the vertical (radian)
μ	dynamic viscosity (N s/m^2)
μ_t	eddy viscosity (N s/m^2)
v	kinematic viscosity (m^2/s)
v_t	eddy viscosity (m^2/s)
ρ	density (kg/m^3)
ρ'	temperature dependent density (kg/m^3)
$\sigma_k, \sigma_\varepsilon$	turbulence constants for the RNG k–ε model
τ	shear stress (N/m^2)

steady-state flow employing the standard k-turbulent model and box-like BTMs.

Of interest here are the experimentally validated CFD simulations of transient turbulent non-isothermal flow with gaseous pollutant transport in a personal exposure environment. The purpose of this paper is to examine the effect of transient breathing on trace gas ambient (i.e., exposure) concentrations and uptake (i.e., dose) concentrations.

2. Theory

Assuming a unidirectional turbulent flow field, the exposure chamber, a realistically looking manikin, and a pollutant source are modeled as shown in Fig. 1. The flow field and contaminant distribution around a person in a ventilated room depend on the system configuration, e.g., ventilation system, location of the person in the room, breathing pattern of the person, local obstacles, heat sources, as well as contaminant sources. The present system generates a near-uniform air flow field which is acceptable for scientific dosimetry-and-health-effect studies, neglecting local pollutant depletion and/or temporal changes in air delivery. A uniform velocity condition ($U_{in} = 0.15$ m/s) with a room temperature ($T = 293.15$ K) is applied at the inlet with a Reynolds number (Re_{D_h}) of 17,583 based on the hydraulic diameter (D_h). One inert point trace gas source is installed at variable heights near the chamber inlet and modeled by uniform non-buoyant gas injection through a 0.1 m diameter porous rubber ball. The specific system set-up is representative and internationally used for test data collection and comparison purposes.

The point source height is most critical when it corresponds to the height of the BTMs mouth as tested by Brohus [14] and is equal to $h_{mouth} = 1.6$ m. The heat transfer boundary condition for the BTMs surface is taken as a convective heat flux of 25 W/ m^2, which corresponds to a moderate activity level of a standing person. By choosing more realistically a heat flux boundary condition instead of a constant wall temperature is also more advantages because it makes the heat transfer from the BTMs surface mesh independent.

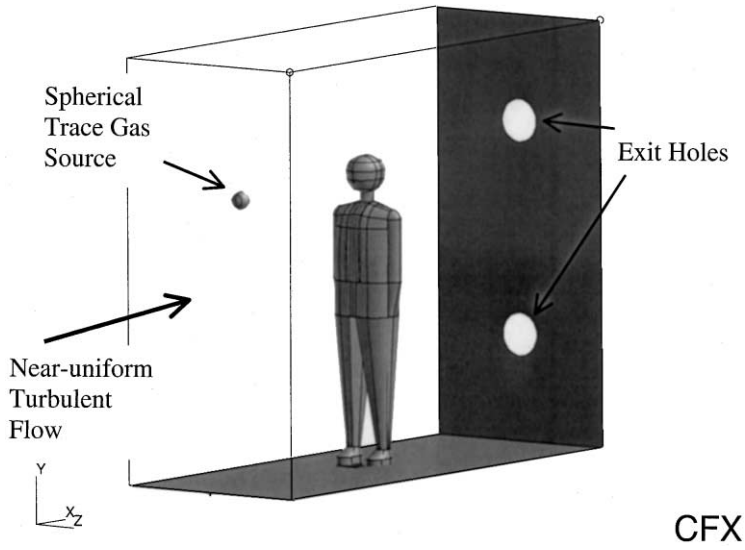

Fig. 1. Computational model for a standard test room, spherical tracer gas source, and realistic subject, a BTM.

The influence of natural convection in this unidirectional chamber flow is measurable, where the Richardson number $Ri = Gr/Re^2$ is in the range of $0 < Ri \leqslant 23.0$. Hence, mixed convention analysis should be applied to solve for this system.

To evaluate the personal exposure/dose, a mouth opening with a total area of 1.3 cm^2 is generated. For the steady-state calculations, the constant inhalation for a person at moderate exercise is applied, i.e., the constant speed of the inhalation is used based on an air intake rate of 30 l/min. For transient simulations, the breathing pattern for a moderate active level of standing is applied (cf. Fig. 2) with a tidal volume equal to 1091 ml during the breathing period of $T = 3.871$ s.

The results for the personal dose/exposure and spatial trace gas concentrations are presented in dimensionless form regarding the personal exposure/dose to make them more general and independent of the specific pollutant gas source strength. Thus, the dimensionless parameter for the personal dose or exposure, C_{d}^*, is defined as

$$C_{\mathrm{d}}^* = \frac{C_{\mathrm{d}} \cdot \hat{Q}}{S_{\mathrm{p}}} = \frac{C_{\mathrm{d}}}{C_{\mathrm{ex}}}. \tag{1}$$

2.1. Governing equations

The basic assumptions for the CFD simulations include fully turbulent non-isothermal incompressible flow. The industry standard for turbulence simulation is the κ–ε model because of its robustness at a relatively low computational cost; however, it is a poor predictor of flow separation [15]. Considering the relatively complex geometry of the BTM model and the need for accurate fine scale modeling, the ReNormalization Group (RNG) κ–ε model, which reportedly can accurately predict flow separation and reattachment [3,15,16], has been selected. The transport equations for incompressible turbulent flow employing the RNG procedure of Yakhot and Orszag [17] are in tensor notation [18]

$$\frac{\partial u_i}{\partial x_i} = 0 \tag{2}$$

and

$$\frac{\partial u_i}{\partial t} + u_i \frac{\partial u_i}{\partial x_j} = -\frac{1}{\rho}\frac{\partial p}{\partial x_i} + \frac{\partial}{\partial x_j}\left[(\nu + \nu_{\mathrm{t}})\left(\frac{\partial u_i}{\partial x_j} + \frac{\partial u_j}{\partial x_i}\right)\right] + \frac{f_j}{\rho}, \tag{3a}$$

where

$$\nu_{\mathrm{t}} = C_\mu \frac{k^2}{\varepsilon} \tag{3b}$$

with

$$k = \frac{1}{2}\overline{u_i' u_i'} \tag{3c}$$

and

$$\varepsilon = \nu \overline{\frac{\partial u_i'}{\partial x_j}\frac{\partial u_i'}{\partial x_j}}. \tag{3d}$$

Calculation of the turbulent kinetic energy, k, and dissipation rate, ε, requires two additional partial differential equations [18] which contain four unknown coefficients in addition to C_μ of Eq. (3b). Using the RNG methodology [16,17], these "constants" are determined as

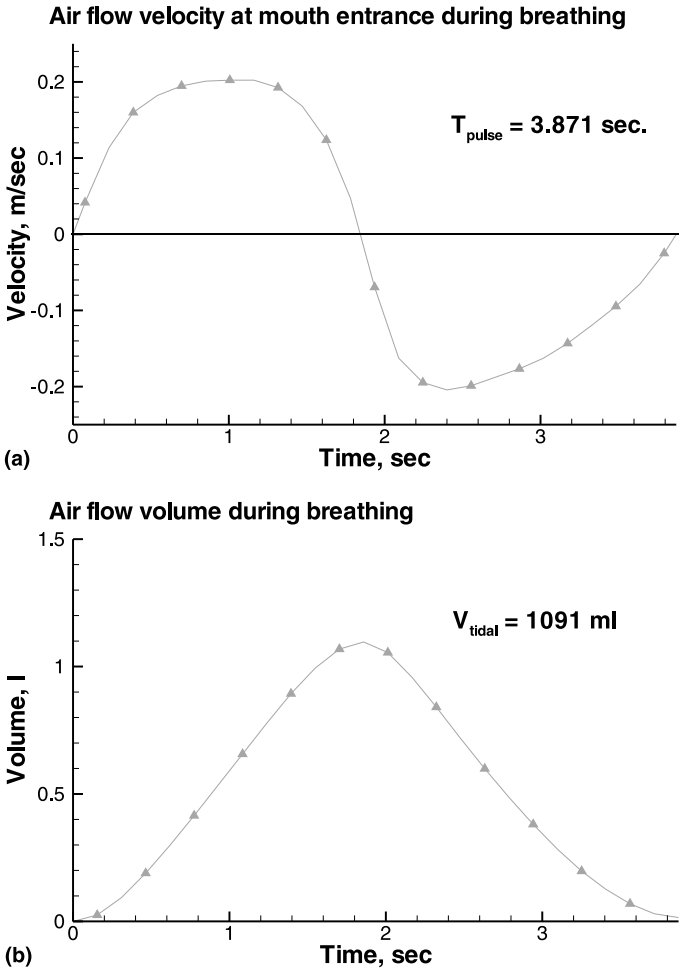

Fig. 2. Representative breathing waveform and tidal volume.

$$C_\mu = 0.085, \tag{4a}$$

$$C_{\varepsilon 1} = 1.42 - \frac{\eta(1-\eta/\eta_\infty)}{1+\beta\eta^3}, \tag{4b}$$

$$C_{\varepsilon 2} = 1.68, \tag{4c}$$

$$\delta_k = 0.7179, \tag{4d}$$

$$\delta_\varepsilon = 0.7179, \tag{4e}$$

where

$$\eta = S_t \cdot k/\varepsilon, \tag{5a}$$

$$\eta_\infty = 4.38, \tag{5b}$$

$$\beta = 0.015, \tag{5c}$$

$$S_t = (2\bar{S}_{ij}\bar{S}_{ij})^{1/2} \tag{5d}$$

and $\bar{S}_{ij}$ is the mean rate-of-strain tensor.

The Boussinesq model is employed for the calculation of the buoyancy force, f_j, where the fluid model density is not dependent on temperature, pressure or additional variables. The local density variation is defined as

$$\rho' = \rho\{1-\beta_t(T-T_{ref})\}, \tag{6}$$

where β_t is the thermal expansion rate, T_{ref} is the buoyancy reference temperature, and ρ is the fluid density. For the temperature distribution calculations, the energy equation can be written as [18]:

$$\frac{\partial(\rho h)}{\partial t} + \frac{\partial}{\partial x_j}(\rho u_j h - q_j) = \frac{\partial p}{\partial t} + \frac{\partial}{\partial x_j}(u_i \tau_{ij}). \tag{7}$$

The Reynolds-averaged mass transport equation can be written as [18]

$$\frac{\partial(\rho Y_{CO})}{\partial t}+\frac{\partial(\rho u_j Y_{CO})}{\partial x_j}-\frac{\partial}{\partial x_j}\left[\left(\rho D_{CO}+\frac{\mu_t}{Sc_t}\right)\frac{\partial Y_{CO}}{\partial x_j}\right]=S, \tag{8}$$

where the turbulent Schmidt number (Sc_t) is of the order of one and S represents the sink/source term used in the gas-uptake analysis.

2.2. Numerical method

The numerical solution of the Eulerian transport equations were carried out with a user-enhanced, unstructured finite-volume based program CFX 5.3 (AEA Technology, UK), with fast turn-around times, good robustness, and rapid convergence. CFX 5.3 employs an unstructured control volume mesh with triangular meshes on the surface of the geometry, which reproduces complex geometries in the computational finite volume domain. Thus, using CFX 5.3, more complex system geometries can be discretized using CAD software as a pre-processor. There was a wide range of length scales for the chamber with a BTM. For example, at the mouth of the BTM, the cell size was as small as $\Delta s = 0.002$ m, while for the open chamber $\Delta s = 2.46$ m.

The mesh size of the computational domain used in this study was adjusted until acceptable levels of grid independence of the solution were achieved. The y^+ for this study was in a range of 0.03 to 16.7, which is small enough for the RNG κ–ε turbulence model. We tested four different computational mesh sizes, i.e., $0.001\ \text{m} \leqslant \Delta s \leqslant 0.02$ m, and the best mesh size $s = 0.002$ for the occupied chamber simulations generated about 350,000 cells, which resulted in grid-independent and reasonable tracer gas concentration values.. The computations were performed on an SGI Origin 2000 workstation with multi-processors located at the North Carolina Supercomputing Center (RTP, NC). The computational time required for the steady-state flow simulation was approximately 12 h.

The convergence criteria for the acceptable level of error in the steady–steady as well as transient analyses are the normalized residual and the global conservation imbalance, which provide a way of establishing how well conservation has been maintained. For this study, if the normalized residuals for all variables were below 1.0E-04 and the global conservation imbalance for the hydrodynamic equations were less than 1%, then the solution was assumed to be converged.

For the inlet boundary condition, the standard test room with the spherical tracer gas source and realistic breathing manikin were modeled (cf. Fig. 1) assuming steady or transient, incompressible, three-dimensional, isotropic turbulent flow and smooth walls. A fully developed turbulent velocity profile representing an inlet air stream with $U_{in} = 0.15$ m/s, a (room) temperature ($T = 293.15$ K), a homogeneous kinetic turbulence energy, k, of 4.6204×10^{-5} m^2/s^2, and a turbulence dissipation rate, ε, of 3.6505×10^{-7} m^2/s^3 was incorporated. The fully developed boundary condition, which is a zero normal pressure gradient, was applied to two exit ports (cf. Fig. 1). For the transient simulations, the results from the steady-state simulation were used as the initial condition for all variables. At the mouth of the inhaling BTM, a uniform velocity was applied based on the breathing pattern shown in Fig. 2. We assumed that the inlet turbulence intensity ($I = u'/U$) was 0.037, which is an appropriate value for internal pipe flows. The transient inlet turbulence kinetic energy (κ) and the transient turbulence dissipation (ε) at the BTMs mouth can be calculated as follows:

$$k_{inlet} = \frac{3}{2} I^2 u^2 \tag{9a}$$

$$\varepsilon_{inlet} = \frac{k_{inlet}^{3/2}}{0.3 \times D_h}, \tag{9b}$$

where D_h is the hydraulic diameter of the inlet. For the heat transfer simulations, an adiabatic wall boundary condition was applied to the chamber walls and a constant heat transfer coefficient was taken for the BTMs surface. It was assumed that the exhaled air had a trace gas concentration of 0.

3. Results

3.1. Model validation

Brohus [14] measured the exposure concentration of a trace gas contaminant using a steadily inhaling BTM and calculated the trace gas concentration distribution using a simple box model. The present flow conditions are exactly the same as his experimental conditions but the BTM is more realistically generated.

The inhaled dose concentration is non-dimensionalized via the return concentration which is an average contaminant concentration at the chamber exit, i.e., $C_d^* = C_d/C_{ex}$. Fig. 3 shows the inhaled non-dimensional dose concentration with and without heat generated by the BTM. The computational data points (C_d^*) agree with the measurements of Brohus [14]. With buoyancy effects, the maximum dose concentration is shown at an elevated source height when compared to the ''no-heat''case, and the maximum value of the dimensionless dose concentration for the ''heat-on''-case is less than that for the ''heat-off''case. Here, the critical point source height is about 1.6 m; hence, for the present analysis $h_{BTM} = 1.7$ m and $h_{mouth} = 1.6$ m as well.

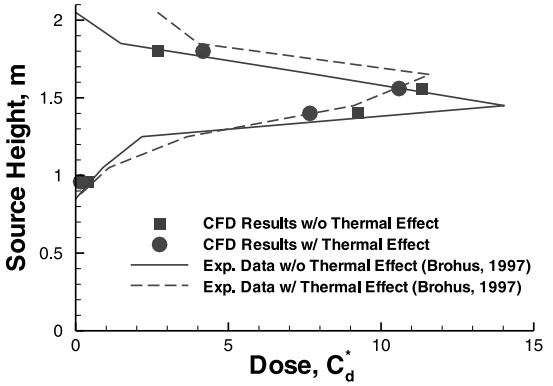

Fig. 3. Data comparison for personal dose of the BTM standing in a unidirectional flow field.

3.2. Velocity fields

All air flow field graphs are shown for constant inhalation ($u_{\text{mouth}} = 0.1$ m/s) by the subject (or BTM) for easy comparison and in form of unit velocity vectors with gray shades indicating speed. Figs. 4(a)–(d) show the velocity vector fields for an inlet Reynolds number of 17,583 with and without heat generation by the BTM in the vertical midplane ($z = 0$) and the horizontal plane at breathing level ($y = 1.6$ m). In comparing Figs. 4(c) and (d) with 4(a) and (b), considerable thermal effects can be seen. Specifically, strong buoyant flows exist as thermal boundary layers behind the BTM (cf. Fig. 4(c)) and in form of counter-rotating vortices which are attached to the subject's body (cf. Figs. 4)(b) and (d). Thermal effects alter the

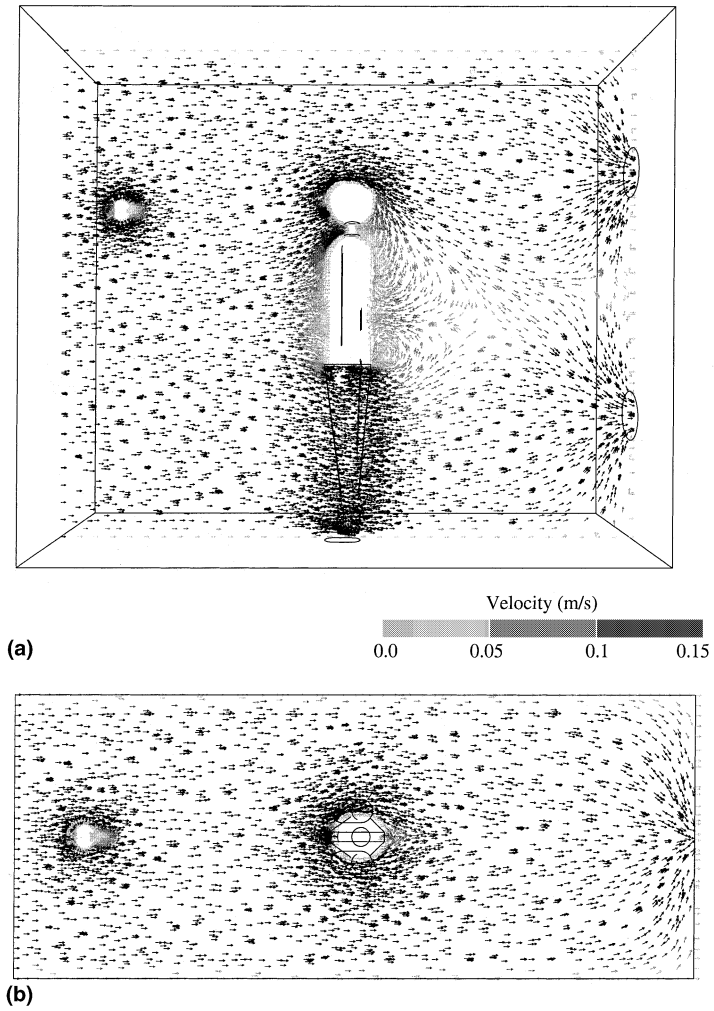

Fig. 4. Steady-state unit velocity vector fields for the zero-degree rotation case (BTM facing turbulent air stream): (a) vertical symmetry plane without heat generation; (b) horizontal plane at breathing level without heat generation; (c) vertical symmetry plane with BTM heat generation; and (d) horizontal plane at breathing level with heat generation.

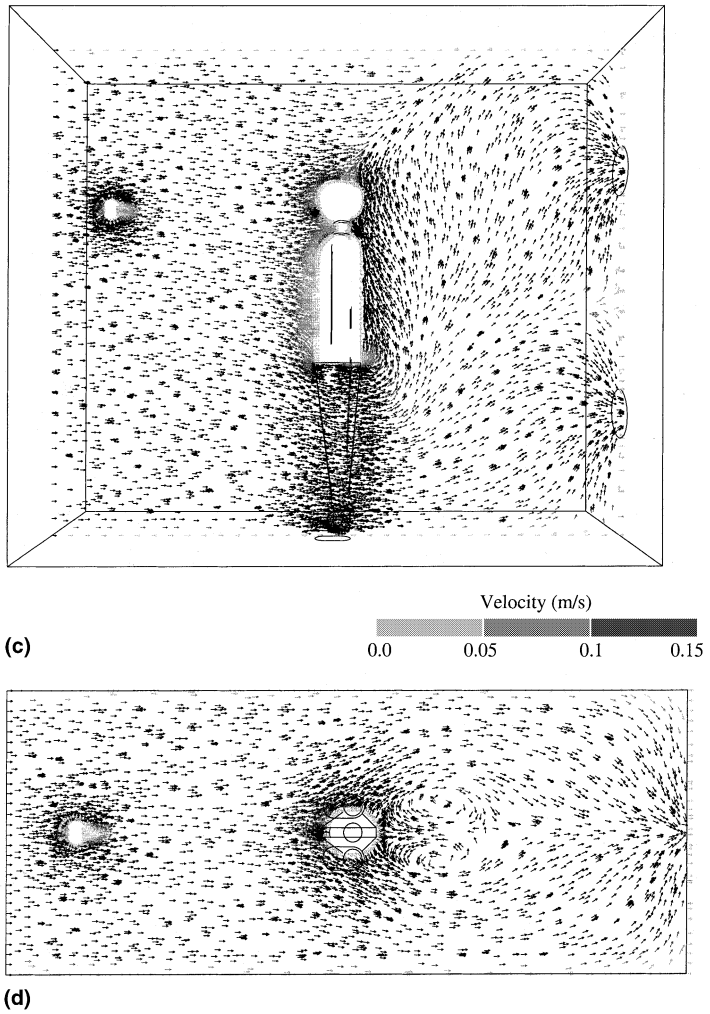

Fig. 4 (*continued*)

flow field around the subject, where air is entrained from the lower downstream region, generating a "plume"behind the BTM. The air speed at the back of the BTM with heat generation is faster than that without heat generation (cf. Figs. 4(a) vs. 4(c)) and no vortical flow is observed in the vertical midplane (cf. Fig. 4(c)). The vortices attached to the subject's head with heat generation are larger than those for the isothermal case.

Figs. 5 and 6 represent the unit velocity vector fields in the midplane ($z = 0$) and the horizontal plane at breathing level ($y = 1.6$ m) for different BTM orientations with respect to the free stream flow or x-direction. Upstream velocity fields for both cases are similar to that for the previous zero-degree rotation case (cf. Figs. 4(c) and 4(d)). For the 90°-rotation case (Figs. 5(a) and (b)), the buoyant flow starts near the BTMs feet and extends to the BTMs head. The vortical flow region attached to the BTM is smaller than that in the previous case because the body's cross-sectional area facing the air stream is less than that for the 0°-and 180°-rotation cases. Due to a much weaker buoyant flow near the BTM, a thermal plume is not observed.

The velocity vector field for the 180°-rotation case is similar to that for the 0°-rotation case except near the BTMs head (cf. Figs. 6(a) and (b) and 4(c) and (d)). The constant inhalation removes some air from the buoyant flow field and prevents the generation of a plume above the BTMs head (Fig. 6) when compared to the 0°-rotation case (cf. Fig. 4(c)). Also, this constant inhalation reduces the size of the vortices attached to the BTMs head (cf. Figs. 6(d) and 4(d)). The buoyant flow ascending from the lower body could reach the BTMs breathing zone, affecting the degree of tracer gas inhalation.

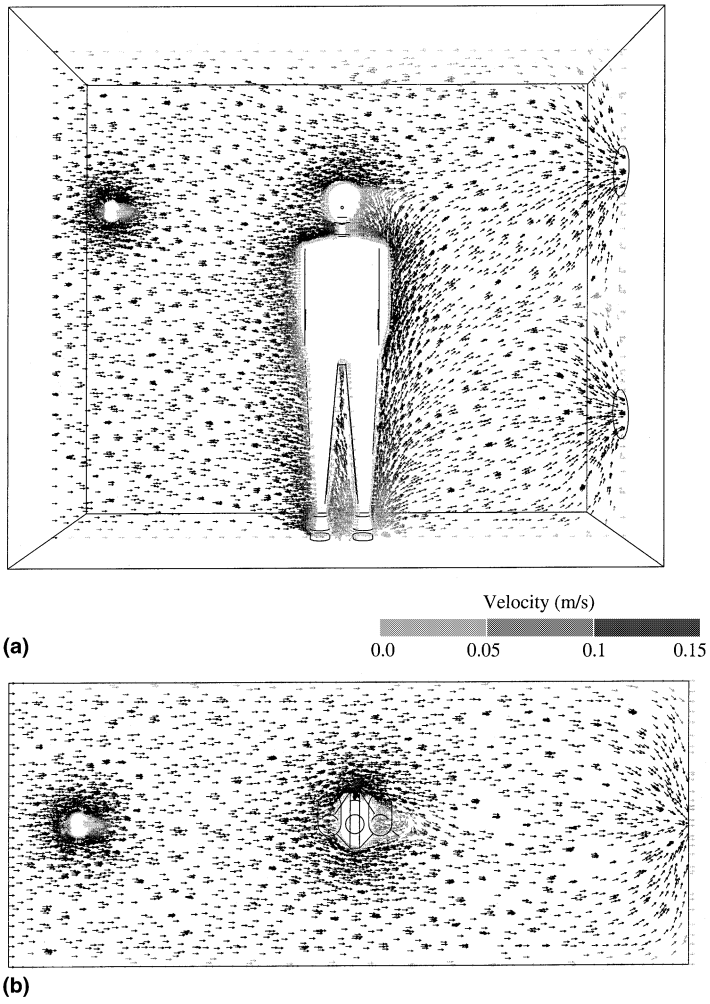

Fig. 5. Steady-state unit velocity vector fields for the 90°-rotation case: (a) vertical symmetry plane with heat generation; and (b) horizontal plane at breathing level with heat generation.

3.3. Temperature Fields

Figs. 7–9 show the steady-state temperature contours for different BTM orientations. For all cases, a higher temperature is observed near flow separation and stagnation and inside the attached vortices (cf. Figs. 4–6) because heat cannot be dissipated easily in these regions with relatively low air speed. Areas of higher velocities are associated with lower body temperatures but flows with higher air temperatures, for example from lower regions of the body, may cause elevated body temperatures. Typically, the upstream air temperature as well as the speed of the surrounding airflow are the important factors to determine the body temperature under the uniform heat flux boundary condition.

In the present case, the mean air temperatures entering the BTMs mouth for the 0°-rotation case (cf. Fig. 7), for the 90°-rotation case (cf. Fig. 8), and for the 180°-rotation case (cf. Fig. 9) are 294.3, 294.3, and 295.4 K, respectively. The slightly higher mean temperature in the last case is due to the BTMs mouth orientation which connects to the thermal plume region (cf. Figs. 4(c), (d) and 9).

3.4. Steady-state tracer gas concentrations

Figs. 10(a)–(c) represent the steady-state nondimensional tracer gas concentration contours as the results of a passive point source located upstream for different BTM orientations. The tracer gas source height is equal to the breathing level, i.e., $h_{\text{mouth}} = 1.6$ m. The upstream side of the BTMs body is exposed to high tracer gas concentrations but the back area has very low concentrations except for the 90°-rotation case. For the 0°-

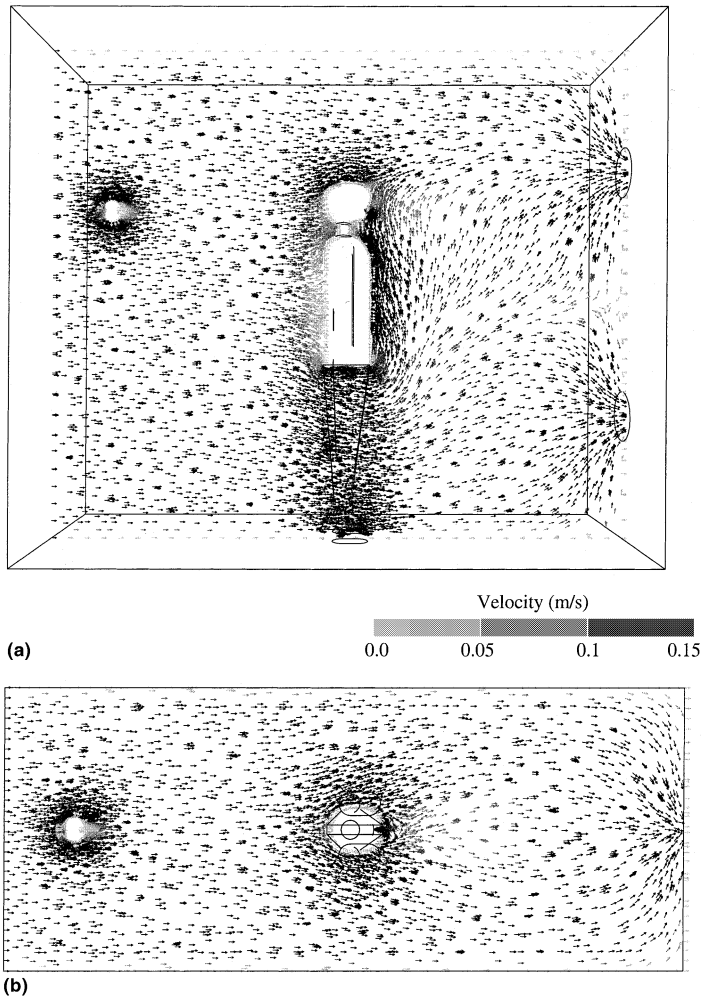

Fig. 6. Steady-state unit velocity vector fields for the 180°-rotation case: (a) vertical symmetry plane with heat generation; (b) horizontal plane at breathing level with heat generation.

rotation case (Fig. 10(a)), relatively high tracer gas concentrations are being directly inhaled, somewhat diluted by the thermal boundary layer and plume discussed in conjunction with Figs. 4(c) and (d). The steady-state personal dose, $C^*_{d,st}$, is calculated as 10.59 and is very close to the measurement by Brohus [15], which was 10.0. Fig. 10(b) shows the tracer gas concentration contours for the 90°-rotation case. The upstream contours are similar to those for the previous case (cf. Fig. 10(a)), but the tracer gas depletion is less because of the weaker buoyant flow. However, the mouth location/orientation is outside of the high tracer gas concentration region. As a result, the steady-state personal dose, $C^*_{d,st}$, is about half, i.e., 5.44. For the 180°-rotation case (Fig. 10(c)), buoyant flow with lower tracer gas concentrations reaches the mouth of the BTM and the steadystate personal dose, $C^*_{d,st}$, is quite low at 0.48.

3.5. Transient tracer gas concentrations

Considering realistic inhalation (cf. Fig. 2), the transient non-dimensionalized dose concentration, $C^*_d(t)$, is shown for: (i) axial air flow moving towards the face of the breathing subject, (ii) axial air flow moving towards the side of the face of the breathing subject, and (iii) axial air flow approaching the back of the breathing subject (Figs. 11(a)–(c)). For the 0°-rotation case, the cyclic patterns of $C^*_d(t)$ do not change much because of the strong axial flow supplying consistently tracer gas to the subject's face. At the beginning of inhalation, $C^*_d(t)$ starts with a very low value and increases because some of the exhaled air recirculates; however, most of the inhaled air is supplied from the chamber inlet. Hence, the time-averaged dose concentration, $\overline{C^*_d} = \frac{1}{T}\int C^*_d(t)\,dt$, is less than the dose concentration for the steady-inhalation-only

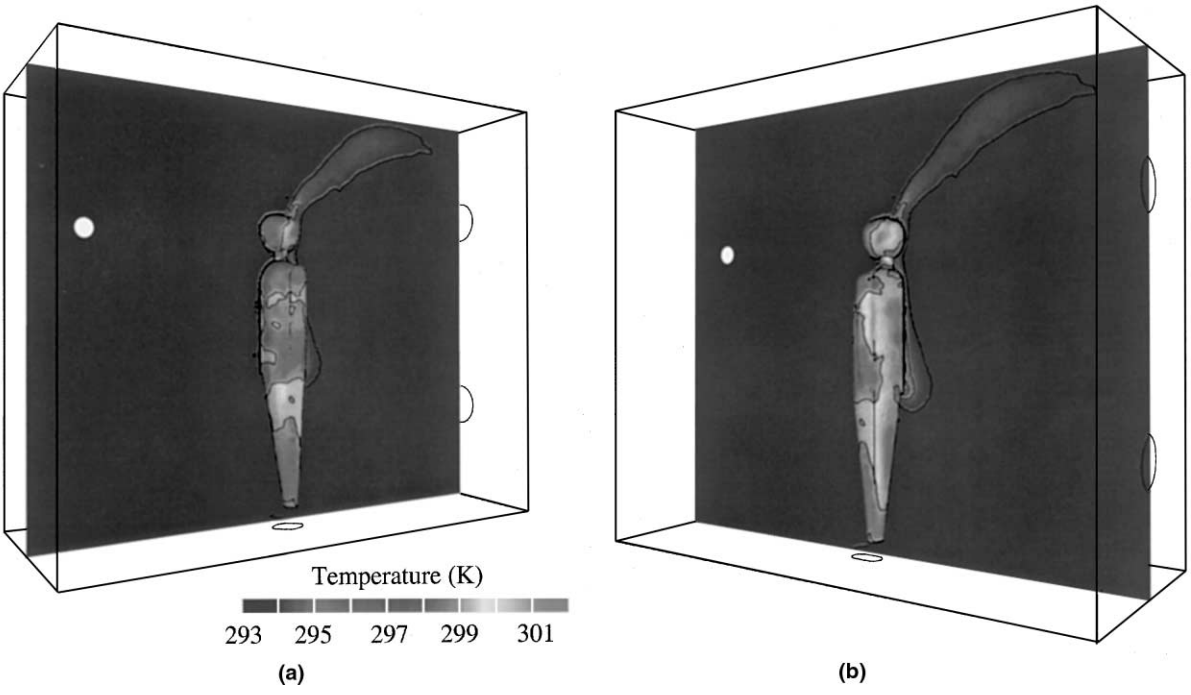

Fig. 7. Two-sided system view and temperature contours for the 0°-rotation case.

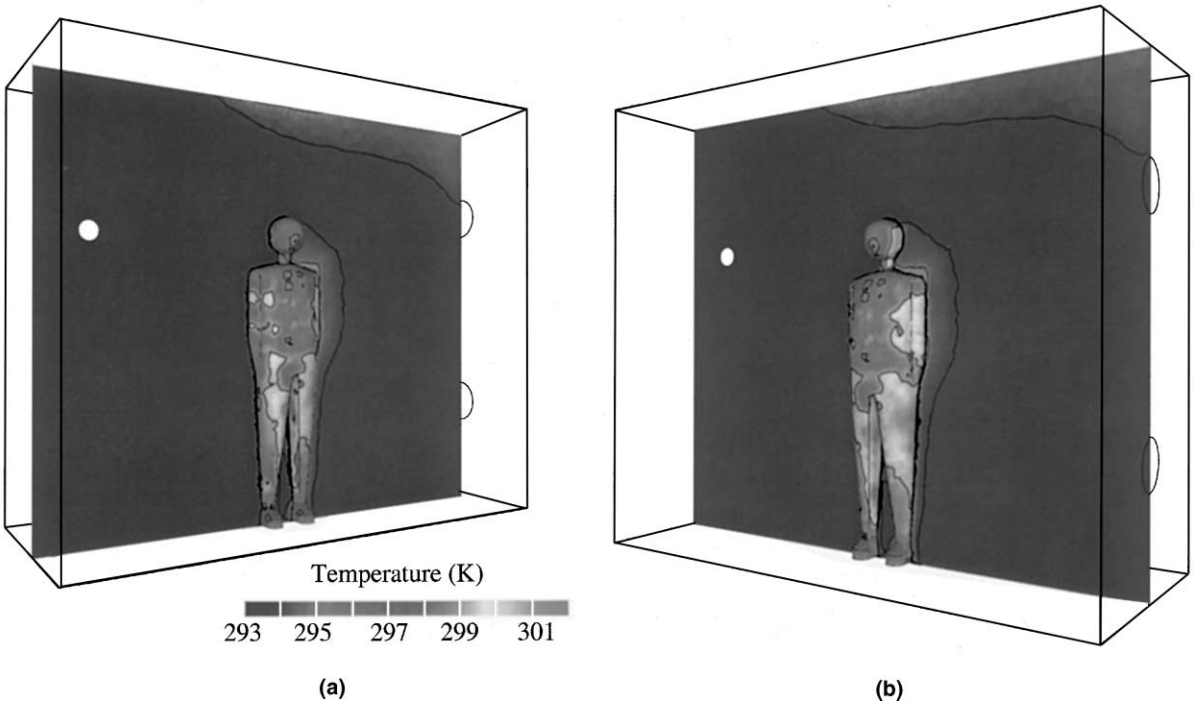

Fig. 8. Two-sided system view and temperature contours for the 90°-rotation case.

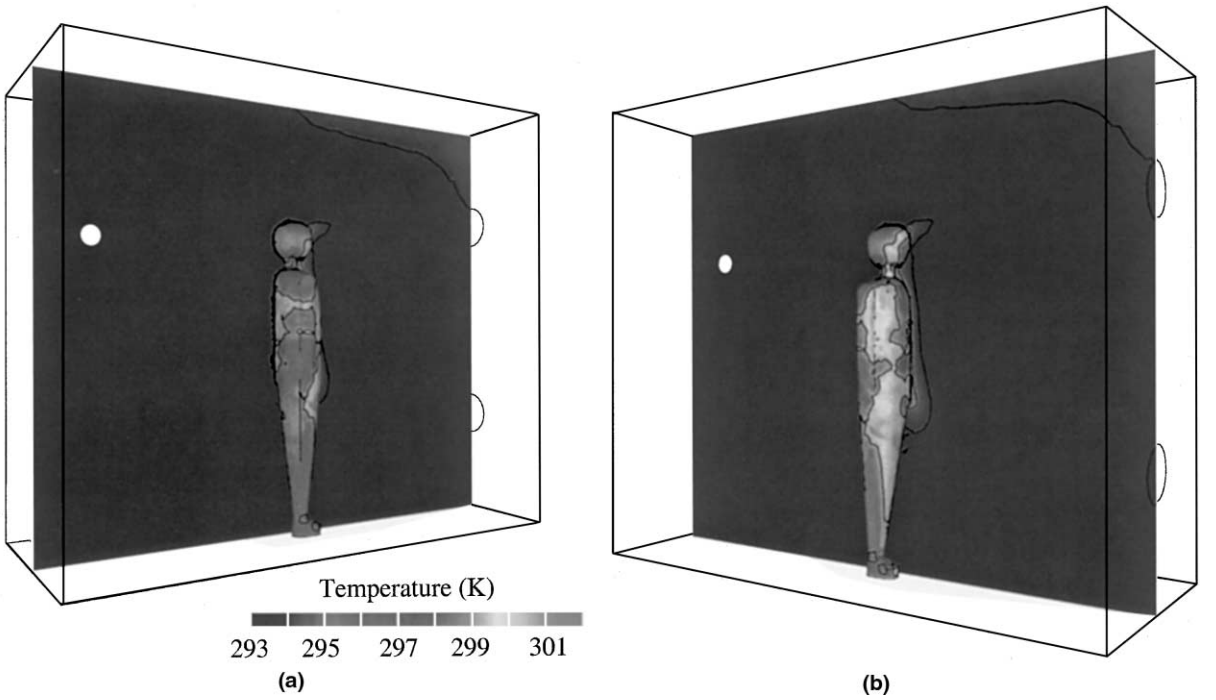

Fig. 9. Two-sided system view and temperature contours for the 180°-rotation case.

case, $C^*_{d,st}$. For the 90°-rotation case, $C^*_d(t)$ is increasing with each cycle. However, buoyant air with lower tracer gas concentrations moves upward reaching the BTMs mouth and as a result, $C^*_d(t)$ is lower than in the previous case. For the 180°-rotation case, $C^*_d(t)$ is relatively high at the beginning and converges to the quasi-steady state concentration because recirculating flow persists in front of the face. Due to the buoyant flow and a wake formed behind the body, air moving upward is stronger than for the 90°-rotation case and hence air with a rather low tracer gas concentration flows towards the subject's mouth. In addition, the pollution concentration in the wake region decreases due to mixing of the inlet flow with the exhaled (zero tracer gas) air as well as buoyant airflow of near-zero trace gas concentrations. The significant reduction in $C^*_d(t)$, $\overline{C^*_d}$ and $C^*_{d,st}$-values for the last case in the presence of a point source, is mainly due to a combination of "clean air"-streams in the wake region which is partly also the breathing zone. Obviously, many more simulations are needed to reach a quasi-steady distribution for the 90°-rotation case.

4. Discussion

Previous CFD studies related to indoor air quality prediction [6,12–14], were based on steady-state simulations and lacking advanced turbulence modeling as well as fine mesh resolutions especially around any occupant. In this paper, the RNG κ–ϵ model has been employed to simulate transient three-dimensional turbulent flow, an unstructured finite volume mesh was developed to represent the detailed surface changes of a breathing thermal manikin (BTM), and transient flow simulations were used to model realistic inhalation/exhalation.

Three different cases have been considered to investigate the effects of flow direction with respect to the BTM orientation on ambient dose concentrations and uptake concentrations. The location of the pollutant gas source and the orientation of the BTM in the flow field mainly influence the tracer gas dose concentration. Especially, for the base case, i.e., 0°-rotation case, the height of the pollutant gas source is important. As expected, the BTM is exposed to the maximum pollutant gas concentration when the height of the pollutant source is about the same as the breathing level, i.e., $h_{mouth} \approx 1.6$ m. However, for the 180°-rotation case, the dose concentration for the lower pollutant gas source height could be higher than that for the breathing level pollutant gas source because the buoyant flow transports air from the lower body side to the upper region, including the subject's mouth.

There is a measurable difference between exposure concentration and dose concentration as well as between

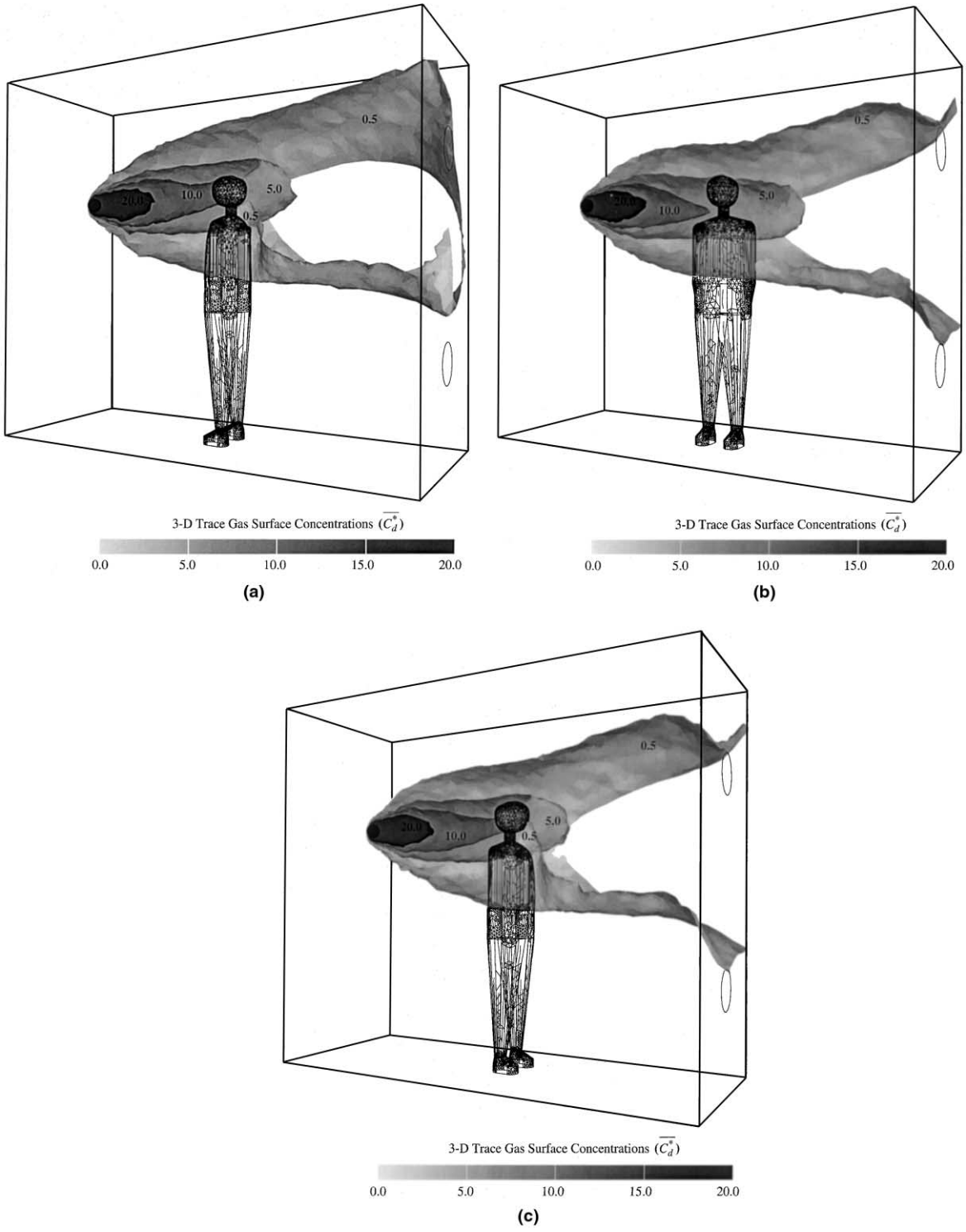

Fig. 10. Steady-state tracer gas concentration contours: (a) the 0°-rotation case; (b) the 90°-rotation case; and (c) the 180°-rotation case.

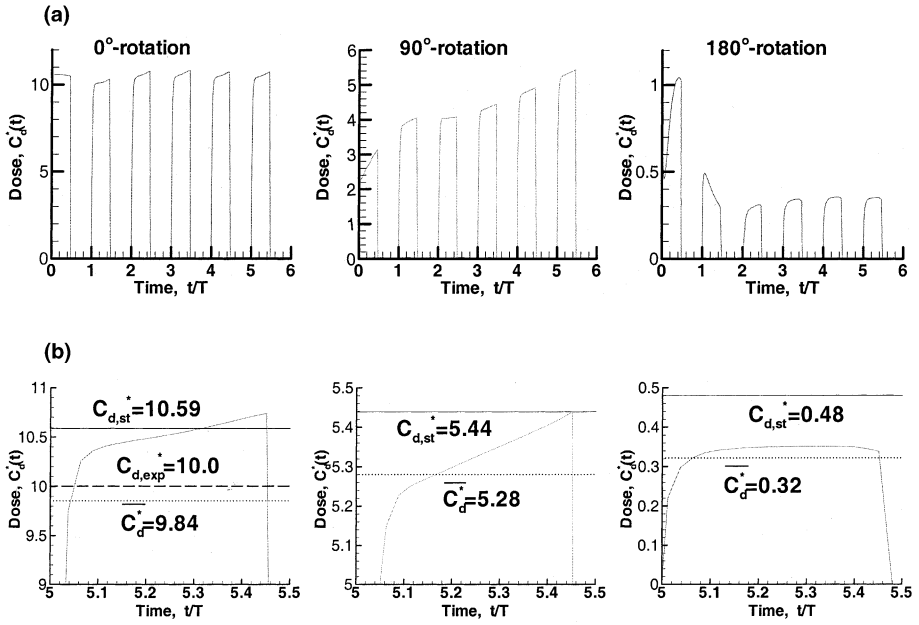

Fig. 11. Transient and time-averaged personal dose concentrations of the BTM with different orientation.

steady-state and transient dose concentrations. Usually, the transient dose concentration is lower than the steady-state dose concentration; however, it depends upon the surrounding flow conditions. Steady-state, i.e., constant inhalation, dose concentrations can be used as the exposure concentration, which is not affected by exhalation. If there are attached recirculation or wake regions near the face or buoyancy influence, it is necessary to simulate the transient system until a quasi-steady dose pattern is reached, i.e., steady-state simulations cannot be applied. The present CFD simulation results are of interest for indoor air quality analyses and control as well as for scientific dosimetry-and-health-effect studies.

Acknowledgements

The authors wish to thank AEA Technology (Bethel Park, PA) and North Carolina Supercomputing Center (RTP, NC) for their support.

References

[1] K.L. Yerkes, A. Faghri, An experimental and numerical simulation of mixed convection in large baffled rectangular chambers, Int. J. Heat Mass Transfer 34 (6) (1991) 1525–1542.

[2] K.L. Yerkes, A. Faghri, Mixed convection analysis in large baffled rectangular chambers with internal heat sources, Int. J. Heat Mass Transfer 35 (5) (1992) 1209–1228.

[3] P.W. Longest, C. Kleinstreuer, J. Kinsey, Turbulent three-dimensional air flow and trace gas distribution in an inhalation test chamber, ASME J. Fluids Eng. 122 (2) (2000) 403–411.

[4] M. Maroni, Health effects of indoor air pollutions and their mitigation and control, Rad. Prot. Dosimetry 78 (1) (1998) 27–32.

[5] S. Hyun, C. Kleinstreuer, Computational Exposure and Dose Assessment Analyses for Transient Turbulent Flow and Gaseous Pollutant Transport, Roomvent 2000, Reading, UK, 2000.

[6] E. Bøjrn E, P.V. Nielsen, Exposure Due to Interacting Air Flows Between Persons, Roomvent '96, 1996, pp. 107–114.

[7] H.B. Awbi, Ventilation of Buildings, Chapman & Hall, London, 1991.

[8] P.V. Nielsen, Computational fluid dynamics in ventilation, Ph.D. Thesis, Aalborg University, Denmark, 1994.

[9] M. Andersen, Particle movements in mechanically ventilated piggeries, Ph.D. Thesis, The Royal Veterinary and Agricultural University, Copenhagen, Denmark, 1995.

[10] C. Topps, P.V. Nielsen, P. Heiselberg, L.E. Sparks, E.M. Howard, M. Mason, Experiments on Evaporative Emissions in Ventilated Rooms, Roomvent '98, 1998, pp. 499–505.

[11] M. Mattson, M. Sandberg, Displacement ventilation – influence of physical activity, Rad. Prot. Dosimetry 78 (1) (1998) 78–92.

[12] E. Bøjrn, P.V. Nielsen, Passive Smoking in a Displacement Ventilated Room, Indoor Air '96, 1996, pp. 887–892.

[13] E. Bøjrn, P.V. Nielsen, CFD Simulations of Contaminant Transport between Two Breathing Persons, Roomvent '98, 1998, pp. 133–140.

[14] H. Brohus, Personal exposure to contaminant sources in ventilated rooms, Ph.D. Thesis, Aalborg University, Denmark, 1997.

[15] P.A. Durbin, Separated flow computations with the κ–ε-v^2 model. AIAA J. 33 (4) (1004) 659–664.
[16] C.G. Speziale, S. Thangam, Analysis of an RNG based turbulence model for separated flows, Int. J. Eng. Sci. 30 (10) (1992) 1379–1388.
[17] V. Yakhot, S.A. Orzag, Renormalization group analysis of turbulence. I. Basic theory, J. Sci. Comput. 1 (1996) 3–51.
[18] C. Kleinstreuer, Engineering Fluid Dynamics An Interdisciplinary Systems Approach, Cambridge University Press, New York, 1997.